

Measurement of Spin-Density Matrix Elements in $\Delta^{++}(1232)$ photoproduction

F. Afzal^{d*}, C. S. Akondiⁱ, M. Albrecht^{aa}, M. Amarian^x, S. Arrigo^{ag}, V. Arroyaveⁱ, A. Asaturyan^{aa}, A. Austregesilo^{aa}, Z. Baldwin^e, F. Barbosa^{aa}, J. Barlow^{ij,z}, E. Barriga^{ij}, R. Barsotti^o, D. Barton^x, V. Baturin^x, V. V. Berdnikov^{aa}, T. Black^w, W. Boeglinⁱ, M. Boer^{ae}, W. J. Briscoe^{ik}, T. Britton^{aa}, S. Cao^j, E. Chudakov^{aa}, G. Chung^{ae}, P. L. Cole^{iq}, O. Cortes^k, V. Crede^{ij}, M. M. Dalton^{aa}, D. Darulis^{il}, A. Deur^{aa}, S. Dobbs^{ij}, A. Dolgolenko^{ip}, M. Dugger^{ia}, R. Dzhygadlo^m, D. Ebersole^{ij}, M. Edo^g, H. Egiyan^{aa}, T. Erbori^{ij}, P. Eugenio^{ij}, A. Fabrizi^r, C. Fanelli^{ag}, S. Fangⁱⁿ, J. Fitches^{il}, A. M. Foda^m, S. Furletov^{aa}, L. Gan^w, H. Gao^h, A. Gardner^a, A. Gasparian^v, D. Glazier^{il}, C. Gleason^{ad}, V. S. Goryachev^{ip}, B. Grube^{aa}, J. Guo^{ie}, L. Guoⁱ, J. Hernandez^{ij}, K. Hernandez^a, N. D. Hoffman^{ie}, D. Hornidge^{it}, G. Houⁿ, P. Hurck^{il}, A. Hurley^{ag}, W. Imoehl^{ie}, D. G. Ireland^{il}, M. M. Ito^{ij}, I. Jaegle^{aa}, N. S. Jarvis^{ie}, T. Jeske^{aa}, M. Jingⁿ, R. T. Jones^{ig}, V. Kakoyan^{ai}, G. Kalicy^f, V. Khachatryan^o, C. Kourkoulis^{ib}, A. LaDuke^e, I. Larin^{aa}, D. Lawrence^{aa}, D. I. Lersch^{aa}, H. Li^{ag}, B. Liuⁱⁿ, K. Livingston^{il}, G. J. Lolos^y, L. Lorenti^{ag}, V. Lyubovitskij^{iac,ab}, R. Maⁿ, D. Mack^{aa}, A. Mahmood^y, H. Marukyan^{ai}, V. Matveev^{ip}, M. McCaughan^{aa}, M. McCracken^{ie,af}, C. A. Meyer^{ie}, R. Miskimen^{ir}, R. E. Mitchell^{io}, K. Mizutani^{aa}, V. Neelamana^y, L. Ng^{aa}, E. Nissen^{aa}, S. Orešić^y, A. I. Ostrovidov^j, Z. Papandreou^y, C. Paudel^{ij}, R. Pedroni^v, L. Pentchev^{aa}, K. J. Peters^m, E. Prather^g, S. Rakshit^{ij}, J. Reinhold^{ij}, A. Remington^{ij}, B. G. Ritchie^{ia}, J. Ritman^{im,c}, G. Rodriguez^{ij}, D. Romanov^s, K. Saldana^o, C. Salgado^u, S. Schadmand^{im}, A. M. Schertz^{io}, K. Scheuer^{ag}, A. Schick^r, A. Schmidt^{ik}, R. A. Schumacher^{ie}, J. Schwiening^{im}, N. Septian^{ij}, P. Sharp^{ik}, X. Shenⁱⁿ, M. R. Shepherd^{io}, J. Sikes^o, A. Smith^{aa}, E. S. Smith^{ag}, D. I. Sober^f, A. Somov^{aa}, S. Somov^s, J. R. Stevens^{ag}, I. I. Strakovsky^{ik}, B. Sumner^a, K. Suresh^{ag}, V. V. Tarasov^{ip}, S. Taylor^{aa}, A. Teymurazyan^y, A. Thiel^{id}, T. Viducic^{ix}, T. Whitlatch^{aa}, N. Wickramaarachchi^{if}, Y. Wunderlich^{id}, B. Yu^h, J. Zarling^y, Z. Zhang^{ah}, X. Zhou^{ah}, B. Zihlmann^{aa}

^aPolytechnic Sciences and Mathematics, School of Applied Sciences and Arts, Arizona State University, Tempe, Arizona, 85287, USA

^bDepartment of Physics, National and Kapodistrian University of Athens, 15771, Athens, Greece

^cRuhr-Universität-Bochum, Institut für Experimentalphysik, D-44801, Bochum, Germany

^dHelmholtz-Institut für Strahlen- und Kernphysik, Universität Bonn, D-53115, Bonn, Germany

^eDepartment of Physics, Carnegie Mellon University, Pittsburgh, Pennsylvania, 15213, USA

^fDepartment of Physics The Catholic University of America, Washington, D.C. 20064, USA

^gDepartment of Physics, University of Connecticut, Storrs, Connecticut, 06269, USA

^hDepartment of Physics, Duke University, Durham, North Carolina, 27708, USA

ⁱDepartment of Physics, Florida International University, Miami, Florida, 33199, USA

^jDepartment of Physics, Florida State University, Tallahassee, Florida, 32306, USA

^kDepartment of Physics, The George Washington University, Washington, D.C., 20052, USA

^lSchool of Physics and Astronomy, University of Glasgow, Glasgow, G12 8QQ, United Kingdom

^mGSI Helmholtzzentrum für Schwerionenforschung GmbH, D-64291, Darmstadt, Germany

ⁿInstitute of High Energy Physics, Beijing, 100049, People's Republic of China

^oDepartment of Physics, Indiana University, Bloomington, Indiana, 47405, USA

^pNational Research Centre Kurchatov Institute, Moscow, 123182, Russia

^qDepartment of Physics, Lamar University, Beaumont, Texas, 77710, USA

^rDepartment of Physics, University of Massachusetts, Amherst, Massachusetts, 01003, USA

^sNational Research Nuclear University Moscow Engineering Physics Institute, Moscow, 115409, Russia

^tDepartment of Physics, Mount Allison University, Sackville, New Brunswick, E4L 1E6, Canada

^uDepartment of Physics, Norfolk State University, Norfolk, Virginia, 23504, USA

^vDepartment of Physics, North Carolina A&T State University, Greensboro, North Carolina, 27411, USA

^wDepartment of Physics and Physical Oceanography, University of North Carolina at Wilmington, Wilmington, 28403 USA

^xDepartment of Physics, Old Dominion University, Norfolk, Virginia, 23529, USA

^yDepartment of Physics, University of Regina, Regina, Saskatchewan, S4S 0A2, Canada

^zDepartment of Mathematics, Physics, and Computer Science, Springfield College, Springfield, Massachusetts, 01109, USA

^{aa}Thomas Jefferson National Accelerator Facility, Newport News, Virginia, 23606, USA

^{ab}Laboratory of Particle Physics, Tomsk Polytechnic University, 634050, Tomsk, Russia

^{ac}Department of Physics, Tomsk State University, 634050, Tomsk, Russia

^{ad}Department of Physics and Astronomy, Union College, Schenectady, New York, 12308, USA

^{ae}Department of Physics, Virginia Tech, Blacksburg, VA, 24061, USA

^{af}Department of Physics, Washington & Jefferson College, Washington, Pennsylvania, 15301, USA

^{ag}Department of Physics, William & Mary, Williamsburg, Virginia, 23185, USA

^{ah}School of Physics and Technology, Wuhan University, Wuhan, Hubei, 430072, People's Republic of China

^{ai}A. I. Alikhanyan National Science Laboratory (Yerevan Physics Institute), 0036, Yerevan, Armenia

Abstract

We report the measurement of spin-density matrix elements of the $\Delta^{++}(1232)$ in the photoproduction reaction $\gamma p \rightarrow \pi^- \Delta^{++}(1232)$ with the GlueX experiment in Hall D at Jefferson Lab. The measurement used a linearly polarized photon beam with $E_\gamma = 8.2 - 8.8$ GeV and the statistical precision exceeds the previous measurement from SLAC by three orders of magnitude for the momentum transfer squared region $-t < 1.4$ GeV². The data are sensitive to the previously undetermined relative sign between couplings in existing Regge exchange models. Linear combinations of the extracted SDMEs allow for a decomposition into natural and unnatural exchange amplitudes, which shows that the unnatural exchange plays an important role in the low $-t$ region.

1. Introduction

In recent years, there have been many discoveries in the spectroscopy of exotic hadrons containing both light and heavy quarks that cannot be described as conventional hadrons (mesons and baryons) in the quark model, *e.g.* [1, 2, 3, 4]. The GlueX experiment at Jefferson Lab studies the photoproduction of light-quark mesons and baryons, with an emphasis on the search for one type of these exotic hadrons, namely hybrid mesons. Photoproduction with a linearly polarized photon beam can be described by t -channel Regge exchanges with contributions from natural-parity $P(-1)^J = 1$ (*e.g.* ρ) and unnatural-parity $P(-1)^J = -1$ (*e.g.* π) exchange. In studying the meson spectrum through photoproduction, understanding these exchange mechanisms is important for the development of the amplitude analyses required to search for new states.

The reaction $\gamma p \rightarrow \pi^- \Delta^{++}$ studied here offers the opportunity to investigate the charge exchange mechanism, in particular, the unnatural-parity pion exchange. We report the measurement of spin-density matrix elements (SDMEs) of the $\Delta^{++}(1232)$ for the reaction $\gamma p \rightarrow \pi^- \Delta^{++}(1232)$ with a linearly polarized photon beam with an average beam energy of $E_\gamma = 8.5$ GeV. These SDMEs describe the spin polarization of the spin- $\frac{3}{2}$ Δ^{++} in terms of the underlying helicity amplitudes and can separate contributions from the different parity exchanges.

Two theoretical models have been developed to describe $\pi\Delta$ photoproduction using Regge theory amplitudes by the Joint Physics Analysis Center (JPAC) [5] and Yu and Kong [6]. These models are constrained by previous measurements of the squared four-momentum transfer t dependence of both the differential cross section [7, 8] and linearly-polarized beam asymmetry [8, 9]. There is only one previous measurement of the SDMEs which had limited statistical precision and coverage in t [10]. The measurement presented here provides the first determination of the t -dependence of the SDMEs, which confirms the importance of unnatural-parity exchange in the low $-t$ region. This exchange is not well described by existing models, demonstrating the lack of constraints provided by previous measurements.

2. The GlueX experiment

The data presented here were collected by the GlueX experiment, located in Hall D at Jefferson Lab. The Continuous Electron Beam Accelerator Facility (CEBAF) provided an electron beam of 11.6 GeV energy which was incident on a thin diamond crystal of 50 μm thickness, producing linearly polarized photons via coherent bremsstrahlung. The coherent peak was placed at the incoming photon energy of $E_\gamma = 8.8$ GeV, giving a polarization degree of about 28-36% in the range between $E_\gamma = 8.2 - 8.8$ GeV. The degree of linear polarization was measured with a triplet polarimeter [11] and has an estimated systematic uncertainty of 1.5%. To reduce systematic effects, the diamond orientation was changed regularly between two pairs

of orthogonal linear polarization angles: 0° , 90° and 45° , -45° . A tagging system, consisting of a dipole magnet and scintillation detectors placed in the tagger focal plane, measured the scattered electrons' momenta determining the energy and production time of the bremsstrahlung photon beam.

The photon beam impinged on a 30 cm-long liquid hydrogen target, surrounded by a detector system consisting of a Start Counter (SC) [12], Central [13] and Forward Drift Chambers (CDC and FDC), as well as Barrel [14] and Forward Calorimeters (BCAL and FCAL) and a forward time-of-flight (TOF) detector. A superconducting solenoid magnet with an average field strength of 2 T surrounds the central detectors. Photons are detected with a high angular acceptance from $1^\circ - 120^\circ$ in polar angle and full azimuthal acceptance in the two calorimeters BCAL and FCAL, while charged particles are tracked in the CDC and FDC, providing a momentum resolution of 1-5%. In addition, time-of-flight measurement and the energy loss dE/dx measurement in the CDC can be used for particle identification. More details about the setup are given in [15].

The results presented here are obtained from the first phase of the GlueX experiment, with data collected in 2017 and 2018, with a total integrated luminosity of about 125 pb^{-1} in the coherent peak region.

3. Spin-density matrix elements (SDMEs)

3.1. Event Selection

The reaction $\gamma p \rightarrow \pi^- \Delta^{++}(1232)$ was studied, where the $\Delta^{++}(1232)$ decays to $\pi^+ p$. Exclusive events with the $\pi^- \pi^+ p$ final state topology were selected by imposing several requirements on the data. Events with at least two positively charged particles and one negatively charged particle were used for the analysis and each possible combination of these particles was analyzed. Events with up to three additional charged tracks were allowed to avoid rejecting signal events with spurious uncorrelated (or random) tracks. The proton and charged pion candidates were identified by time-of-flight requirements using the charged particle timing information from the SC, BCAL, FCAL and TOF detectors and energy loss dE/dx in the CDC.

Incident beam photons were required to have an energy in the coherent peak, $E_\gamma = 8.2 - 8.8$ GeV, as measured by the tagger. Using the total initial and final state momenta p_i and p_f , a cut on the measured missing mass squared of $m_{\text{miss}}^2 = |p_i - p_f|^2 < 0.1 \text{ GeV}^2$ was applied, thus, removing events where massive particles were not detected. In addition, a kinematic fit to the reaction hypothesis $\gamma p \rightarrow \pi^- \pi^+ p$ was applied for each event, imposing energy and momentum conservation, as well as a common vertex for all particles. Events were retained that fulfill a kinematic fit convergence of $\chi^2/\text{ndf} < 8.7$.

The initial state beam photon and the final state particles should be coincident in time. The electron beam was provided by the CEBAF accelerator in beam bunches 4 ns apart. The precise bunch time is given by the accelerator radiofrequency (RF) clock. Due to the high-intensity electron beam, multiple tagger hits can be assigned to the same beam bunch, despite only one beam photon interacting with the liquid hydrogen target and triggering the event. The time difference between the

*afzal@jlab.org

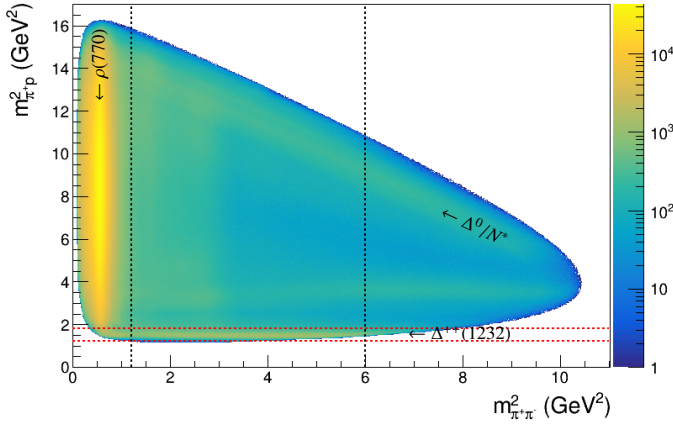


Figure 1: Dalitz plot of the reaction $\gamma p \rightarrow \pi^- \pi^+ p$. The vertical bands show contributions from the $\pi^- \pi^+$ meson system e.g. $\rho(770)$, while the horizontal bands show the $\Delta^{++}(1232)$ and excited states that decay to $\pi^+ p$. On the diagonal, baryon contributions from N^*/Δ^{0*} are visible in the $\pi^- p$ system. The dashed black and red lines show the chosen cuts on the $\pi^- \pi^+$ and $\pi^+ p$ masses, respectively.

final state particles and the tagged beam bunch is required to be less than 2 ns. To account for accidental tagger hits, four beam bunches before and after the prompt peak signal were used with a weight of $-\frac{1}{8}$ to subtract the accidental time background underneath the prompt peak signal in the data sample. This accidental time background makes up roughly 30% of the selected data sample (e.g. Fig. 2 red filled histograms).

The Dalitz plot for this channel is shown in Fig. 1. The $\Delta^{++}(1232)$ was selected with a cut on the $\pi^+ p$ invariant mass of $1.1 < m_{\pi^+ p} < 1.35$ GeV (see Fig. 2a and 2b). The upper cut limit was chosen to avoid significant contribution from higher mass excited Δ^* states. Permutations of the final state particles $\pi^- \pi^+ p$, can lead to background contribution from the $\pi^- p$ baryon system or from the $\pi^- \pi^+$ meson system. The $\pi^- p$ baryon system, consisting of N^*/Δ^{0*} baryon resonances, is seen on the diagonal of the Dalitz plot in Fig. 1. Restricting the analysis to the range of squared four-momentum transfer $t = (p_\gamma - p_\pi)^2$ below 1.4 GeV², removes most of this background. In addition, this background is well separated from the selected $\Delta^{++}(1232)$ mass region in $m_{\pi^+ p}$ and can therefore be neglected. However, the background contribution from the $\pi^- \pi^+$ meson system poses a significant background, as shown in Fig. 1, where the $\rho(770)$ dominates. The $\rho(770)$ contribution can be reduced to a minimum by restricting the $\pi^- \pi^+$ mass range to $1.1 < m_{\pi^- \pi^+} < 2.45$ GeV. The upper cut limit keeps the contribution from excited Δ^* low. Despite the applied cut on the $\pi^- \pi^+$ mass, a significant non-reducible amount of background remains that needs to be taken into consideration. The $\pi^- \pi^+$ background was parameterized by a Bernstein polynomial of 4th degree, as shown in the $m_{\pi^- \pi^+}$ distributions of Fig. 2c and 2d. This background has a $-t$ dependence and amounts to about 20% in the low $-t$ region and reduces to about 10% in the high $-t$ region.

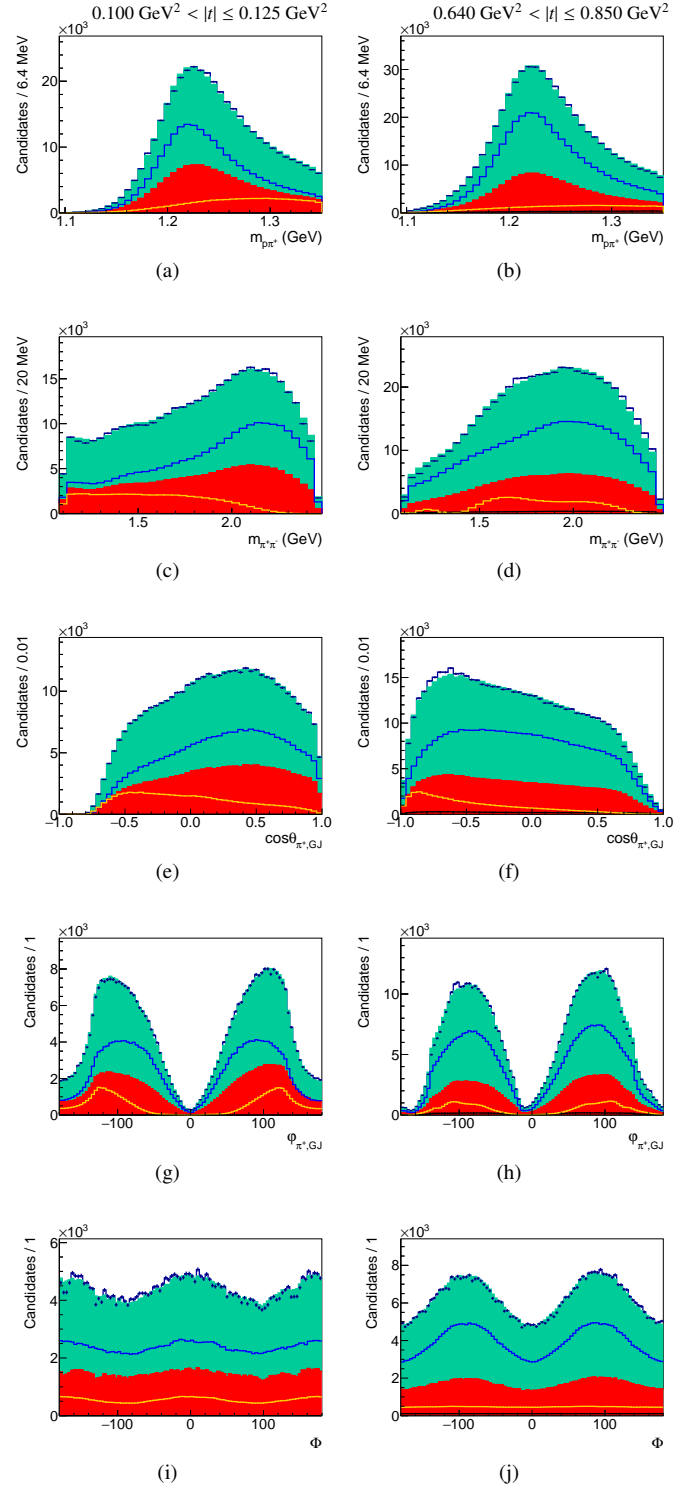


Figure 2: Measured distributions (black points) compared to simulated phase space distributions weighted by the fit results (shaded green area). The accidental time background distribution is depicted as the red shaded area, and the blue, yellow and black lines show $\pi^- \Delta^{++}$, $(\pi^- \pi^+) p$ and phase space contributions, respectively. The left and right columns show results for two representative t bins.

3.2. Extraction of SDMEs

In the photon beam energy range between $8.2 - 8.8$ GeV used in this analysis, the t -channel production process domi-

nates. In order to understand the production mechanism of the $\Delta^{++}(1232)$ recoiling against a π^- and study the charge exchange mechanism, the spin transfer from the linearly polarized photon beam to the $\Delta^{++}(1232)$ can be studied with the help of the spin-density matrix elements (SDMEs). The SDMEs ρ_{ij}^k describe the spin polarization of the $\Delta^{++}(1232)$ and its decay to $\pi^+ p$, where i and j represent two times the spin projection of the Δ^{++} ($i/2, j/2 \in (-3/2, -1/2, 1/2, 3/2)$).

The decay angles of the Δ^{++} were studied in the so-called Gottfried-Jackson (GJ) frame, which is defined in the rest frame of the Δ^{++} with the following coordinate system:

$$\hat{z} = \frac{\vec{p}_{\text{target}}}{|\vec{p}_{\text{target}}|}, \quad \hat{y} = \frac{\vec{p}_\gamma \times \vec{p}_\pi}{|\vec{p}_\gamma \times \vec{p}_\pi|}, \quad \hat{x} = \hat{y} \times \hat{z}, \quad (1)$$

where \vec{p}_{target} , \vec{p}_γ and \vec{p}_π are the 3-momenta of the target proton, beam photon and the π^- in the rest frame of the Δ^{++} .

The formalism describing the spin-density matrix elements for a spin-3/2 particle was previously derived and applied for the $K^+\Lambda(1520)$ final state in an earlier publication [16] and is applied here for the spin-3/2 $\Delta^{++}(1232)$. The measured intensity W depends on three angles: the polar angle $\cos \theta_{\pi^+, GJ}$ and azimuthal angle $\varphi_{\pi^+, GJ}$ of the π^+ in the GJ frame and the angle Φ between the linear polarization vector and the production plane of the Δ^{++} . The linear polarization of the photon beam provides access to ten SDMEs, four unpolarized in Eq. 3 and six polarized in Eq. 4 and 5. To normalize the measured intensity distribution, the relation $\rho_{33}^0 + \rho_{11}^0 = \frac{1}{2}$ was used, reducing the number of independent accessible SDMEs to nine. It should be noted that the definition of the \hat{z} axis in Eq. 1 is defined in the opposite direction to the definition in [16]. This leads to a sign change for the SDMEs of Eq. 5.

$$W(\theta, \varphi, \Phi) = \frac{3}{4\pi} (W^0(\theta, \varphi) - P_\gamma \cos 2\Phi W^1(\theta, \varphi) - P_\gamma \sin 2\Phi W^2(\theta, \varphi)) \quad (2)$$

$$W^0(\theta, \varphi) = \rho_{33}^0 \sin^2 \theta + \rho_{11}^0 \left(\frac{1}{3} + \cos^2 \theta \right) - \frac{2}{\sqrt{3}} \text{Re}[\rho_{31}^0 \cos \varphi \sin 2\theta + \rho_{3-1}^0 \cos 2\varphi \sin^2 \theta] \quad (3)$$

$$W^1(\theta, \varphi) = \rho_{33}^1 \sin^2 \theta + \rho_{11}^1 \left(\frac{1}{3} + \cos^2 \theta \right) - \frac{2}{\sqrt{3}} \text{Re}[\rho_{31}^1 \cos \varphi \sin 2\theta + \rho_{3-1}^1 \cos 2\varphi \sin^2 \theta] \quad (4)$$

$$W^2(\theta, \varphi) = \frac{2}{\sqrt{3}} \text{Im}[\rho_{31}^2 \sin \varphi \sin 2\theta + \rho_{3-1}^2 \sin 2\varphi \sin^2 \theta] \quad (5)$$

The measured intensity distributions were fitted with an extended unbinned maximum likelihood fit using Eq. 2 - 5. The fit method is explained in more detail in [17]. The fit results are evaluated by comparing the data to simulated flat phase-space distributions weighted by the fit results. The phase-space Monte Carlo sample was generated from 3-body phase-space for the $\pi^-\pi^+p$ final state, with acceptance determined with a GEANT4 simulation of the GlueX detector and the same event reconstruction and selection procedures as the data. Figure 2

shows the fit results for two example $|t|$ bins displaying the π^+p and $\pi^-\pi^+$ mass and angular distributions of $\cos \theta_{\pi^+, GJ}$, $\varphi_{\pi^+, GJ}$ and Φ . In addition to the angular dependence of the intensity, a parameterization for the π^+p mass distribution, which shows clearly the $\Delta^{++}(1232)$ peak, was included in the fit. The line shape of the $\Delta^{++}(1232)$ was described with a relativistic Breit-Wigner function, where the mass and the width were considered as floating fit parameters.

3.2.1. Di-pion background parametrization

As mentioned in Section 3.1, the data sample contains an irreducible amount of background stemming from the $\pi^-\pi^+$ meson system. This background contribution is parametrized with a Bernstein polynomial of 4th degree and incoherently added to the signal $\pi^-\pi^+$ contribution. The yellow lines in Fig. 2 show the $\pi^-\pi^+$ background contributions in the mass and angular distributions. The background increases towards higher π^+p mass and shows a strong t -dependence. Since this background may contain meson resonances like excited ρ states it cannot be described by phase-space in the $\pi^-\pi^+$ angular decay distributions, thus a parameterization for the angular dependence was required. We used angular moments to describe the kinematics of the photoproduction of two pseudo-scalar mesons ($\pi^-\pi^+$) as given in [18]:

$$I(\Omega, \Phi) = I^0(\Omega) - P_\gamma I^1(\Omega) \cos 2\Phi - P_\gamma I^2(\Omega) \sin 2\Phi \quad (6)$$

The intensity I of the angular distributions can be decomposed into three different components I^0, I^1 and I^2 , which are given by:

$$I^0(\Omega) = \sum_{L, M \geq 0} \left(\frac{2L+1}{4\pi} \right) (2 - \delta_{M,0}) H^0(LM) d_{M0}^L(\theta) \cos M\varphi \quad (7)$$

$$I^1(\Omega) = - \sum_{L, M \geq 0} \left(\frac{2L+1}{4\pi} \right) (2 - \delta_{M,0}) H^1(LM) d_{M0}^L(\theta) \cos M\varphi \quad (8)$$

$$I^2(\Omega) = \sum_{L, M > 0} \left(\frac{2L+1}{4\pi} \right) \text{Im} H^2(LM) d_{M0}^L(\theta) \sin M\varphi, \quad (9)$$

where $H^\alpha(LM)$ are the moments with $\alpha = 0, 1, 2$, $d_{M0}^L(\theta)$ is the Wigner d -function [19] and Ω consists of the polar angle θ and azimuthal angle φ of π^+ in the helicity frame of the $\pi^-\pi^+$ system as defined in [17]. Truncating the sums in Eq. 7-9 at different L_{max} allowed us to assess the partial-wave content of the $\pi^-\pi^+$ background contribution. We performed fits with $L_{\text{max}} = 0, 2, 4, 6$ and found that a good description of the angular distributions, shown in Fig. 2, is reached when at least S and P wave contributions are considered. Including additional moments corresponding to D -wave contributions slightly improved the description of the data for certain $-t$ bins, and were therefore also considered in the fit using $L_{\text{max}} = 4$. The effects of truncating at $L_{\text{max}} = 4$ and not including F -wave moments were considered in the systematic uncertainty.

In total, 55 fit parameters and three external normalization factors were varied during the extended unbinned maximum likelihood fit for each $-t$ bin: 9 parameters for the Δ^{++} SDMEs,

2 parameters for the lineshape of Δ^{++} , 5 parameters for the Bernstein polynomial to describe the $\pi^-\pi^+$ mass dependence and 39 parameters for the S , P and D wave moments to parameterize the angular dependence of the $\pi^-\pi^+$ background. The three external normalization factors take the three different contributions from $\pi^-\Delta^{++}$, $(\pi^-\pi^+)p$ and phasespace into account.

3.3. Statistical and systematic uncertainty

We determined the statistical uncertainties using the Bootstrapping technique [20] and proceeded in the same way as described in [17].

We considered several contributions to the overall systematic uncertainty of the extracted SDMEs: the chosen event selection criteria for the χ^2/ndf of the kinematic fit and the cuts on the π^+p and $\pi^-\pi^+$ masses, the accuracy of the $\pi^-\pi^+$ background description, the systematic uncertainty of the linear polarization degree and the sensitivity of the detector system to the four different diamond orientations that were used during data-taking.

The influence of the event selection criteria on the extracted SDMEs was taken into account by varying the cut limits and taking the standard deviation of the different fit results with the varied criteria as an estimation for the systematic uncertainty. For the variation of the cuts applied on the χ^2/ndf and m_{π^+p} the total event sample size was not changed by more than 10%. However, since the $\pi^-\pi^+$ background is more significant, the lower cut limit on the $m_{\pi^-\pi^+}$ was varied by up to $m_{\pi^-\pi^+} > 1.7$ GeV which changes the event sample by almost 40%. Despite the large change in the cut limit, the extracted SDMEs remain stable, indicating that the fit model assumptions and results are robust. The absolute systematic uncertainty is on the order of 3×10^{-2} , which represents the second largest contribution to the systematic uncertainty.

In addition, the estimated amount of $\pi^-\pi^+$ background was tested by varying the degree of the Bernstein polynomial stepwise from 3 to 6. Furthermore, the difference between using S , P and D wave moments and using S , P , D and F wave moments for the description of the angular distributions of the $\pi^-\pi^+$ system was taken into account for the systematic uncertainty. The SDMEs ρ_{11}^0 and ρ_{11}^1 are most sensitive to the angular parameterization used for the $\pi^-\pi^+$ background. Both variations account only for a very small part of the overall systematic uncertainty. Apart from using the Bernstein polynomial and angular moments for the $\pi^-\pi^+$ background parametrization, it was also tested to describe the $\pi^-\pi^+$ background using three ρ states, $\rho(770)$, $\rho(1450)$ and $\rho(1700)$ and phasespace for the mass dependence and ρ SDMEs [17] for the angular dependence, which gives consistent results for the Δ^{++} SDMEs within the estimated systematic uncertainty.

A larger contribution to the systematic uncertainty comes from comparing independent fits to the two pairs of orthogonal diamond orientations with their linear polarization direction rotated with respect to the detector system by $(0^\circ, 90^\circ)$ and $(45^\circ, -45^\circ)$, respectively. The deviation between fits to these two independent datasets was assigned as a systematic uncertainty. Finally, the linear polarization degree was varied by its systematic uncertainty of 1.5% and the difference taken into account for the systematic uncertainty.

All sources of systematic uncertainty were added in quadrature to obtain the total systematic uncertainty.

4. Results

4.1. SDMEs

The SDMEs were measured in the GJ frame for 16 independent $-t$ bins and are shown as a function of $-t$ in Fig. 3. The vertical error bars consist of both statistical and systematic uncertainties, which were added in quadrature. The combined uncertainty is dominated by the systematic uncertainty for the entire $-t$ range. The horizontal position of the data points are located at the mean of the $-t$ distribution in the respective $-t$ bin and the horizontal error bars are given by the root mean square value of the $-t$ distribution within that bin. Our results are compared to a previous measurement from SLAC which is reported at $E_\gamma = 9.3$ GeV for one wide $-t \leq 0.4$ GeV² bin [10]. The SLAC data agrees well with our results except for ρ_{31}^0 and ρ_{31}^1 , where deviations outside the given uncertainties of the SLAC data are observed. We report our results in much finer bins of $-t$, allowing us to precisely study the t -dependence of the SDMEs for $-t < 1.4$ GeV² and our results supersede the results of [10].

The results are further compared to predictions of the pole model from the JPAC group [5], which is based on Regge theory amplitudes, taking into consideration pseudo-scalar meson π ($J^{PC} = 0^{-+}$) and axial vector meson b_1 ($J^{PC} = 1^{+-}$) exchange for the unnatural-parity exchange in the t -channel process, while vector meson ρ ($J^{PC} = 1^{--}$) and tensor meson a_2 ($J^{PC} = 2^{++}$) exchanges are expected to play an important role for the natural-parity exchange. The $-t$ dependence for several of the SDMEs ρ_{11}^1 , ρ_{33}^1 , $Re(\rho_{3-1}^0)$ and $Re(\rho_{3-1}^1)$ are, apart from some deviations at lower $-t$, qualitatively in agreement with the JPAC model predictions. However, large discrepancies are visible for the remaining SDMEs. In particular, the model exhibits zero crossings in $Re(\rho_{31}^0)$, $Re(\rho_{31}^1)$ and $Re(\rho_{31}^1)$ at around $-t \approx 0.1$ GeV², which is not observed in the data.

Since the JPAC model predictions were derived first in the helicity frame and later rotated to the GJ frame, we extracted the SDMEs in the helicity frame (see Fig. A.6 in the Appendix) as well and compared them again to the JPAC model. In the helicity frame, the comparison between data and model predictions shows a reasonable, qualitative agreement for all SDMEs. However, the measured SDMEs $Re(\rho_{3-1}^0)$, $Re(\rho_{3-1}^1)$ and $Re(\rho_{3-1}^2)$ have the opposite sign compared to the JPAC pole model predictions. This difference is caused by the relative sign of two helicity amplitude couplings in the JPAC model, which could not be determined from previous measurements of the differential cross section [7, 8] and linearly-polarized beam asymmetry [8, 9], but can now be fixed with our new GlueX data [21]. When rotating the SDMEs to the GJ frame, this sign ambiguity affects all the SDMEs and makes the comparison to the JPAC model more challenging.

The model by Yu and Kong [6] is based on Regge theory as well and considers the t -channel π , ρ and a_2 meson exchanges, however the b_1 meson exchange was not included in

their model since it was not needed to describe previous differential cross section and beam asymmetry data [6]. Overall, the t -dependence of the SDMEs is not well described, demonstrating that our new GlueX data will provide important constraints for the model.

To further investigate the deviations between our data and the model predictions and to separate the unnatural-parity and natural-parity exchanges, linear combinations of SDMEs are discussed in the following section.

4.2. Linear combinations of SDMEs

Linear combinations of the extracted SDMEs can be used to decompose the SDMEs into the unnatural-parity (U) and natural-parity (N) exchange components $\rho_{ij}^{N/U}$:

$$\rho_{ij}^{N/U} = \rho_{ij}^0 \pm \rho_{ij}^1. \quad (10)$$

The relation between $\rho_{ij}^{N/U}$ and the unnatural and natural exchange amplitudes are given in [16]. Figure 4 shows in the top row the natural and in the bottom row the unnatural exchange components. They are compared again to the JPAC pole model and Yu and Kong model predictions. Comparing the top and bottom rows, it becomes evident that in the low $-t$ region up to 0.45 GeV^2 unnatural-parity exchange dominates since in this region the natural ρ_{ij}^N contributions are close to zero, while the unnatural ρ_{ij}^U are large. The situation is reversed for the $-t$ region above 0.45 GeV^2 , where natural-parity exchange dominates. The comparison to the JPAC model reveals that the natural-parity exchange is well modeled by the JPAC pole model. The large deviations between the data and the JPAC pole model, that are visible in the SDMEs in Fig. 3, can be traced back to the unnatural-parity exchange component, where π exchange is assumed to dominate in the t -channel process.

The Yu and Kong model describes the natural-parity exchange well for very low $-t$ values below 0.3 GeV^2 , but cannot predict the t -dependence of the data for larger $-t$ values and either overestimates (ρ_{11}^N and $\text{Re}(\rho_{31}^N)$) or underestimates (ρ_{33}^N and $\text{Re}(\rho_{3-1}^N)$) the natural-parity contributions. The opposite is the case for the unnatural parity-exchange, where the Yu and Kong model does not predict the data well for $-t$ values below 0.3 GeV^2 , but reproduces the data well for higher $-t$ values.

4.3. Beam asymmetry

Using the sum of the two SDMEs ρ_{11}^1 and ρ_{33}^1 , the beam asymmetry Σ can be determined with the following equation:

$$\Sigma = 2(\rho_{11}^1 + \rho_{33}^1). \quad (11)$$

The results for the beam asymmetry are shown in Fig. 5. The results reported here are compared to our previously published results [9], which used only $\sim 17\%$ of the data used in this work, which were extracted using the asymmetry of the event yield for two perpendicular diamond settings and integrating over the Δ^{++} decay angles $\cos \theta_{\pi^+ p, GJ}$ and $\varphi_{\pi^+ p, GJ}$. In general,

both results show a strong $-t$ dependence for the beam asymmetry and are in good agreement within the estimated statistical and systematical uncertainties over a large $-t$ range. However, in the very low $-t$ range, a discrepancy is visible between the two methods. The yield asymmetry method has the disadvantage that it can lead to biased results for Σ in case of a non-uniform detection efficiency of the Δ^{++} decay angles. This bias stemming from the efficiency was taken into consideration for the systematic uncertainty in the previous publication using Monte Carlo simulation based on the JPAC models for the SDMEs, which seems to have been underestimated at low $-t$, where the detection efficiency is highly non-uniform in $\cos \theta_{\pi^+, GJ}$ (see Fig. 2e) and where the JPAC model fail to reproduce the SDMEs ρ_{11}^1 and ρ_{33}^1 well. Our present SDME extraction method for the beam asymmetry according to Eq. 11 does not have any such bias since the full Δ^{++} decay angular phase space is analyzed.

The JPAC pole model describes the t -dependence of the data qualitatively well, but shows large deviations in the magnitude of the beam asymmetry especially in the low $-t$ range. The Yu and Kong model describes the beam asymmetry well in the range above $|t| = 0.5 \text{ GeV}^2$, but does not predict the minimum value well in the low $-t$ range.

5. Summary and conclusions

We report measurements of the $\Delta^{++}(1232)$ SDMEs for the photoproduction reaction $\gamma p \rightarrow \pi^- \Delta^{++}$ that were performed at the GlueX experiment with a linearly polarized photon beam in the incoming photon energy range of $E_\gamma = 8.2 - 8.8 \text{ GeV}$. Our measurements are the first precise determination of the t dependence of the $\Delta^{++}(1232)$ SDMEs. A comparison to the JPAC and Yu and Kong Regge theory models shows that the t -dependence of the SDMEs is not well reproduced, despite the models describing previous unpolarized cross section data and beam asymmetry data from SLAC well. The SDMEs are sensitive to the relative sign of the model couplings, which was undetermined from previous data. Separating the natural-parity and unnatural-parity exchange components through linear combinations of SDMEs revealed that the deviations between data and the JPAC Regge theory model predictions can be traced back to the unnatural-parity exchange component. Thus, the data provide important constraints on the Regge theory models, specifically shedding light on the unnatural-parity pion exchange which is expected to play an important role in many other charge exchange photoproduction reactions to be studied in the search for exotic mesons at GlueX. In particular, the charge exchange reaction $\gamma p \rightarrow \eta' \pi^- \Delta^{++}$ is crucial in attempting to confirm the existence of the lightest hybrid meson $\pi_1(1600)$ based on an estimation of the upper limit for the $\pi_1(1600)$ photoproduction cross section [22].

Acknowledgements

We thank Adam Szczepaniak, Vincent Mathieu, Vanamali Shastry and Gloria Montaña from the JPAC group and B.-G.

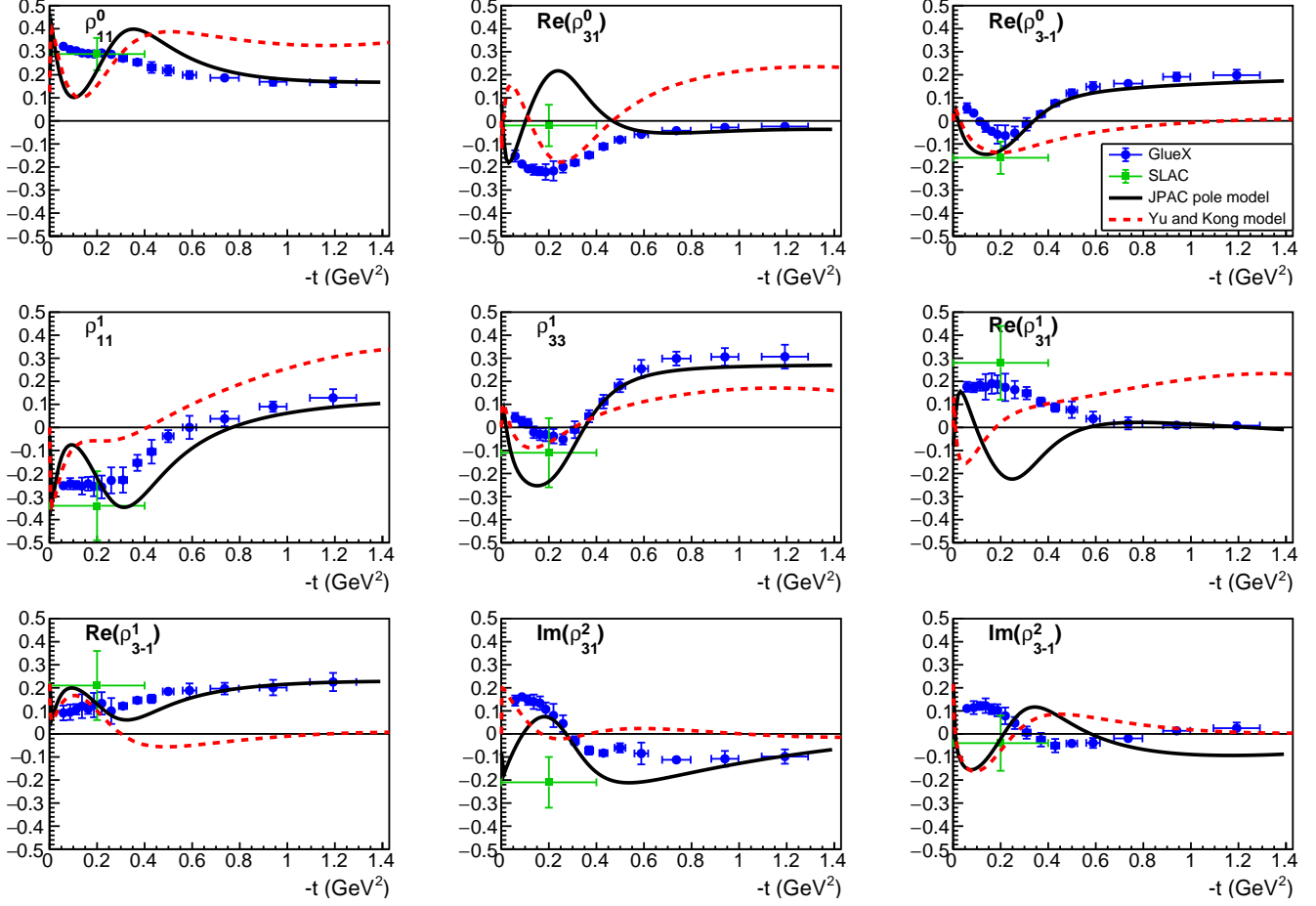


Figure 3: Spin-density matrix elements of Δ^{++} in the Gottfried-Jackson frame (blue points). They are shown as a function of the momentum transfer squared $-t$ from the incoming photon to the π^- . The vertical error bars consist of the statistical and systematic uncertainties combined in quadrature. Our data is compared to the previous SLAC measurement (green square points) [10] and to the JPAC pole model (solid black line) [5] and the Yu and Kong model (dashed red line) [6] predictions.

Yu for the fruitful discussions. The analysis in this article was supported by the U.S. Department of Energy, Office of Science, Office of Nuclear Physics under contract DOE Grant No. DE-FG02-87ER40315. The work of F. Afzal is supported by the Argelander Mobility Grant awarded by the University of Bonn and J. R. Stevens is supported by DOE Grant DE-SC0023978. We would like to acknowledge the outstanding efforts of the staff of the Accelerator and the Physics Divisions at Jefferson Lab that made the experiment possible. This work was also supported in part by the U.S. Department of Energy, the U.S. National Science Foundation, NSERC Canada, the German Research Foundation, GSI Helmholtzzentrum für Schwerionenforschung GmbH, the Russian Foundation for Basic Research, the UK Science and Technology Facilities Council, the Chilean Comisión Nacional de Investigación Científica y Tecnológica, the National Natural Science Foundation of China, and the China Scholarship Council. This material is based upon work supported by the U.S. Department of Energy, Office of Science, Office of Nuclear Physics under contract DE-AC05-06OR23177. This research used resources of the National En-

ergy Research Scientific Computing Center (NERSC), a U.S. Department of Energy Office of Science User Facility operated under Contract No. DE-AC02-05CH11231. This work used the Extreme Science and Engineering Discovery Environment (XSEDE), which is supported by National Science Foundation grant number ACI-1548562. Specifically, it used the Bridges system, which is supported by NSF award number ACI-1445606, at the Pittsburgh Supercomputing Center (PSC).

Appendix A. SDMEs in the helicity frame

Fig. A.6 shows the SDMEs in the helicity frame, which is defined with the following coordinate system in the rest frame of the Δ^{++} :

$$\hat{z} = \frac{-\vec{p}_\pi}{|\vec{p}_\pi|}, \quad \hat{y} = \frac{\vec{p}_\gamma \times \vec{p}_\pi}{|\vec{p}_\gamma \times \vec{p}_\pi|}, \quad \hat{x} = \hat{y} \times \hat{z}. \quad (\text{A.1})$$

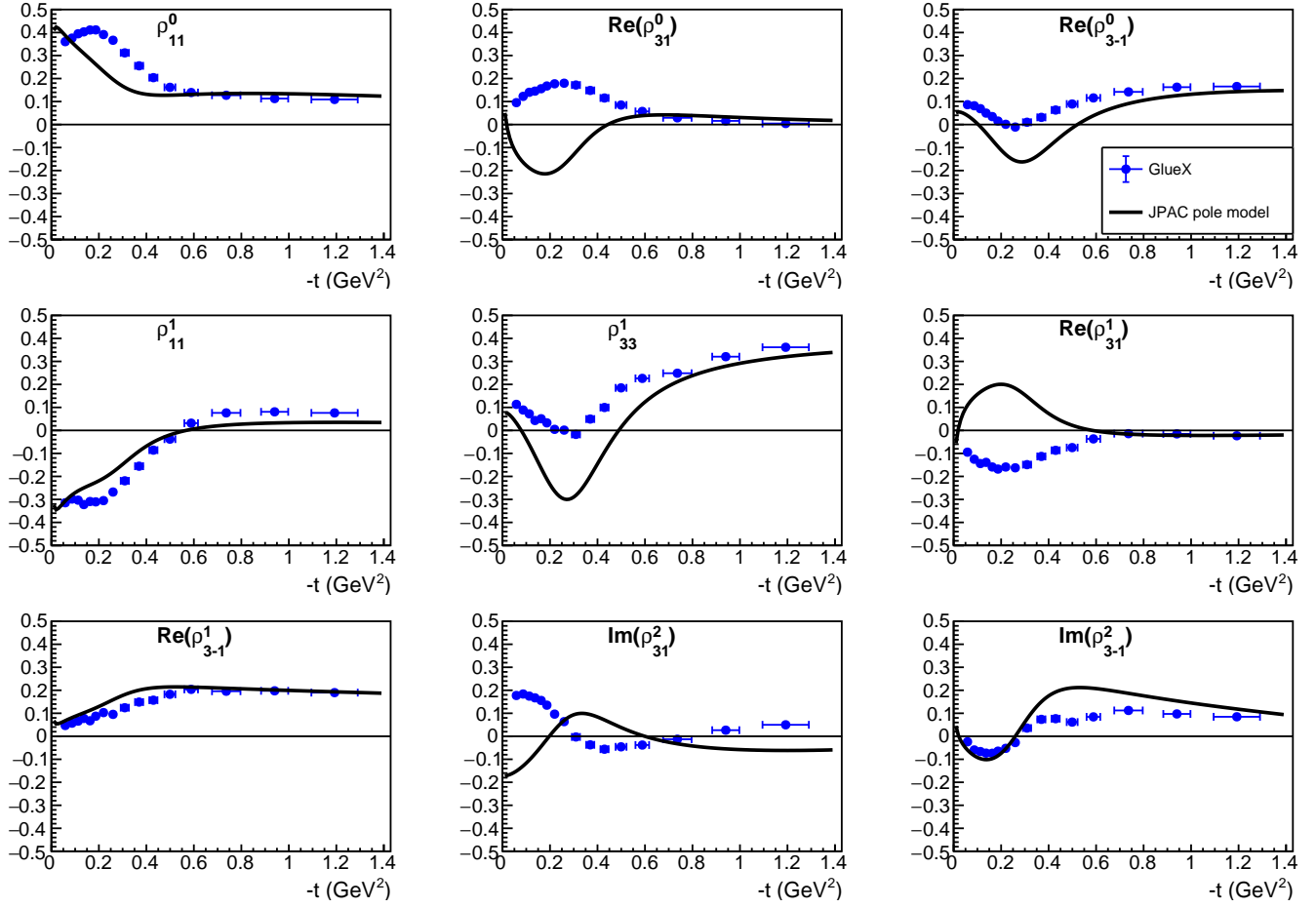


Figure A.6: Spin-density matrix elements of Δ^{++} in the helicity frame (blue points). They are shown as a function of the momentum transfer squared $-t$ from the incoming photon to the π^- . The vertical error bars consist of only the statistical uncertainties. Our data is compared to the JPAC pole model predictions (black solid line) [5].

- trometers, Detectors and Associated Equipment 867 (2017) 115–127. <https://doi.org/10.1016/j.nima.2017.05.026>.
- [12] E. Pooser, et al., The GlueX Start Counter Detector, Nucl. Instrum. Meth. A 927 (2019) 330–342. <https://doi.org/10.1016/j.nima.2019.02.029>. arXiv:1901.02759.
- [13] N. S. Jarvis, et al., The Central Drift Chamber for GlueX, Nucl. Instrum. Meth. A 962 (2020) 163727. <https://doi.org/10.1016/j.nima.2020.163727>. arXiv:1910.07602.
- [14] T. D. Beattie, et al., Construction and Performance of the Barrel Electromagnetic Calorimeter for the GlueX Experiment, Nucl. Instrum. Meth. A 896 (2018) 24–42. <https://doi.org/10.1016/j.nima.2018.04.006>. arXiv:1801.03088.
- [15] S. Adhikari, et al., The GlueX beamline and detector, Nuclear Instruments and Methods in Physics Research Section A: Accelerators, Spectrometers, Detectors and Associated Equipment 987 (2021) 164807. <https://doi.org/10.1016/j.nima.2020.164807>.
- [16] S. Adhikari, et al. (GlueX), Measurement of spin density matrix elements in $\Lambda(1520)$ photoproduction at 8.2–8.8 GeV, Phys. Rev. C 105 (2022) 035201. <https://doi.org/10.1103/PhysRevC.105.035201>. arXiv:2107.12314.
- [17] S. Adhikari, et al. (GlueX), Measurement of spin-density matrix elements in $\rho(770)$ production with a linearly polarized photon beam at $E_\gamma=8.2\text{--}8.8$ GeV, Phys. Rev. C 108 (2023) 055204. <https://doi.org/10.1103/PhysRevC.108.055204>. arXiv:2305.09047.
- [18] V. Mathieu, M. Albaladejo, C. Fernández-Ramírez, A. W. Jackura, M. Mikhasenko, A. Pilloni, A. P. Szczepaniak (Joint Physics Analysis Center Collaboration), Moments of angular distribution and beam asymmetries in $\eta\pi^0$ photoproduction at GlueX, Phys. Rev. D 100 (2019) 054017. <https://doi.org/10.1103/PhysRevD.100.054017>.
- [19] D. A. Varshalovich, A. N. Moskalev, V. K. Khersonsky, Quantum Theory of Angular Momentum: Irreducible Tensors, Spherical Harmonics, Vector Coupling Coefficients, 3nj Symbols, World Scientific, Singapore, 1988.
- [20] B. Efron, R. J. Tibshirani, An introduction to the bootstrap, CRC press, 1994.
- [21] A. Szczepaniak, V. Mathieu, V. Shastri, Private communication, 2024.
- [22] M. Shepherd, Exploring Photoproduction with the GlueX Experiment, EPJ Web Conf. 291 (2024) 01016. <https://doi.org/10.1051/epjconf/202429101016>. arXiv:2311.17826.